

Alejandro Ruiz Martínez

# 3D orientational imaging of gallbladder stones

Graduate thesis in Physics

Supervisor: Basab Chattopadhyay

Co-supervisor: Fredrik K. Mürer

May 2024



Norwegian University of  
Science and Technology



Alejandro Ruiz Martínez

# **3D orientational imaging of gallbladder stones**

Graduate thesis in Physics  
Supervisor: Basab Chattopadhyay  
Co-supervisor: Fredrik K. Mürer  
May 2024

Norwegian University of Science and Technology  
Faculty of Natural Sciences  
Department of Physics





## Preface

This thesis is part of the TFY4561-Physics Project course offered by the Department of Physics at the Norwegian University of Science and Technology (NTNU) in Trondheim, Norway. The supervisors for this work have been Prof. Basab Chattopadhyay (Department of Physics, NTNU) and Fredrik K. Mürer (SINTEF Helgeland).

The main focus of my work has been on the X-ray Diffraction Tensor Tomography (XRD-TT) reconstruction and Propagation Phase-Contrast Computed Tomography (PPC-CT) reconstruction of a gallbladder stone. This could be done thanks to the data obtained from the ID15A beamline at the European Synchrotron Radiation Facility (ESRF) in Grenoble, France.

I would also like to express my gratitude to everyone in the X-ray physics group at NTNU. They not only helped me understand and improve my results but also assisted me with the basics such as accessing and using my data. Thanks to their support and the weekly group meetings, I was able to learn a great deal about recent developments in X-ray physics and imaging techniques, and also gained valuable experience of being part of a research group.

# Contents

<b>1</b>	<b>Introduction</b>	<b>1</b>
1.1	X-ray CT . . . . .	1
1.2	Propagation phase contrast CT . . . . .	2
1.3	X-ray diffraction CT . . . . .	3
1.4	X-ray diffraction TT . . . . .	4
<b>2</b>	<b>Materials and Methods</b>	<b>8</b>
2.1	Gallbladder stones . . . . .	8
2.2	Experimental setup and parameters . . . . .	9
<b>3</b>	<b>Results and Discussion</b>	<b>13</b>
3.1	PPC-CT reconstruction . . . . .	13
3.2	XRD-TT reconstruction . . . . .	16
<b>4</b>	<b>Conclusion</b>	<b>24</b>

### **Abstract**

X-ray Diffraction Tensor Tomography is an emerging imaging technique to study the mineralogy and orientation of crystallites at a microscale level. In the work presented in this thesis, we have tested an algorithm developed for this kind of reconstruction on a gallbladder stone. Additionally, we have compared the Tensor Tomography reconstruction with a Propagation Phase-Contrast Computed Tomography reconstruction, which provides a high-resolution morphological map of the stone's structure. The combination of the two techniques enabled us to investigate the orientation of the cholesterol monohydrate crystals that form the gallstone in relation to its morphology.

# Chapter 1

## Introduction

### 1.1 X-ray CT

X-ray Computed Tomography (XR-CT) is a non-destructive three-dimensional imaging technique based on the interaction of X-rays with matter. Tomography refers to the cross-sectional imaging of an object that can be reconstructed from its projections [1]. The projections are taken with a detector that measures the modified intensity of the X-rays when they traverse the sample. Projections are taken for different orientations of the sample, this means, for different rotation angles around the tomographic axis.

The source for these X-rays can either be an X-ray tube or a synchrotron. Tube sources emit a polychromatic (usually wide and with sharp characteristic peaks depending on the material) spectrum in a cone. For measurements using this type of source, which is the typical one for laboratory and hospital CT, a cone beam set up system as the one depicted in Fig. 1.1a is needed. But, synchrotrons can provide a monochromatic X-ray beam with unparalleled brilliance [2] and tangential to the storage ring, making this source a much more suitable option when high resolution and contrast is needed. Since the source is situated far away from the specimen, the X-rays that arrive to the sample can be considered a parallel beam. The CT experiment presented in this thesis comes from measurements in a synchrotron facility which need of a set up as the one shown in Fig. 1.1b.

XR-CT allows for characterization of materials and it has been widely used in medicine and materials science. XR-CT can come in different forms depending on what is measured or used as image parameter. For instance, the most popular modes for XR-CT are absorption-contrast, phase-contrast, and scattering/diffraction. Every type of CT allows for different application since they provide different resolution and type of information, as well as they are suitable for diverse sample sizes.

X-ray CT can be used to image samples sized up to meters and resolve length scales ranging from millimeters down to tens of nanometers, making it an ideal technique for studying hierarchical materials. For instance, X-ray Diffraction Computed/Tensor Tomography techniques provide a resolution of around tens of micrometers while also capturing information about structures on the scale of tenths of nanometers.

The conventional techniques for XR-CT imaging are attenuation-contrast and phase-contrast. Both of them are based on exploiting refractive index properties of the sample.



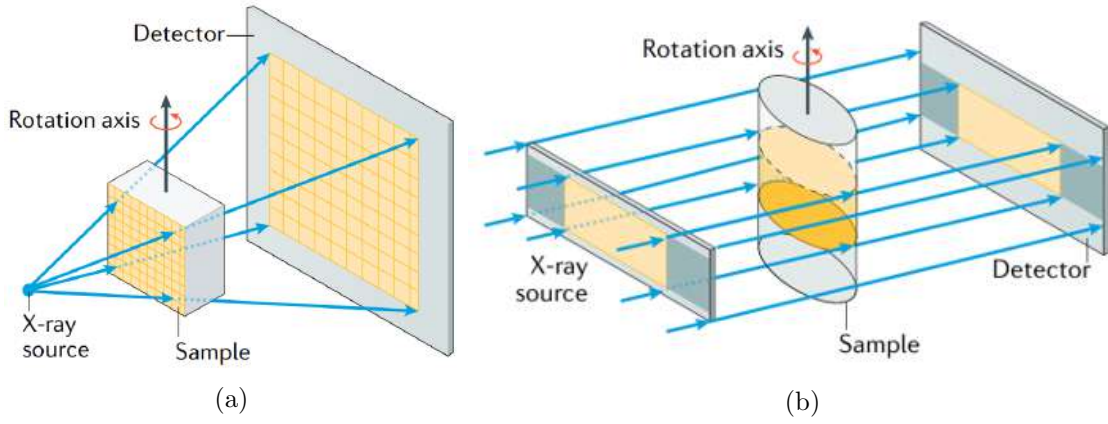


Figure 1.1: (a) Typical experimental set up for laboratory and hospital cone beam geometry CT installation [3]. (b) Typical parallel beam geometry CT experimental set up, used in synchrotron facilities [3].

In general, the refractive index of a material can be written as

$$n = 1 - \delta + i\beta, \quad (1.1)$$

where the real part controls the phase shift, and the imaginary part controls the attenuation [3].

The working principles of the attenuation of X-rays in a material can be described with Beer-Lambert's law [3]

$$\ln(I/I_0) = \int_0^d \mu(x) dx, \quad (1.2)$$

where  $I_0$  and  $I$  are the initial and final intensities, respectively, of an X-ray after going through a distance  $d$  of a material with attenuation coefficient  $\mu(x)$  at each point  $x$ . In general, in a sample,  $\mu$  is dependent on the position (as well as on the energy of the X-rays) but in an homogeneous region the law is reduced to

$$I = I_0 e^{-\mu d}. \quad (1.3)$$

Then, the attenuation coefficient can be identified as  $\mu = k\beta$ , where  $k$  is the wave number of the X-ray, when compared to the form of a plane wave travelling inside a material with imaginary part of the refractive index  $\text{Im}[n] = \beta$ .

## 1.2 Propagation phase contrast CT

For samples with little spatial variation in attenuation properties, it is common to use phase-contrast imaging so that some details that are hidden to attenuation contrast can be revealed by phase contrast CT. In particular, it is common to make use of it in soft tissues since these have a variation of the real part of the refractive index on the order of  $\delta = 10^{-5}$  for X-rays, which is small and difficult to detect.

All of the experimental setups for phase-contrast measurements can schematically be drawn as in Fig. 1.1b in which a parallel beam is used, as it is in the measurements for the work in this thesis. In particular, propagation-based phase-contrast lays on measuring the intensity variations caused by constructive and destructive interference that happen

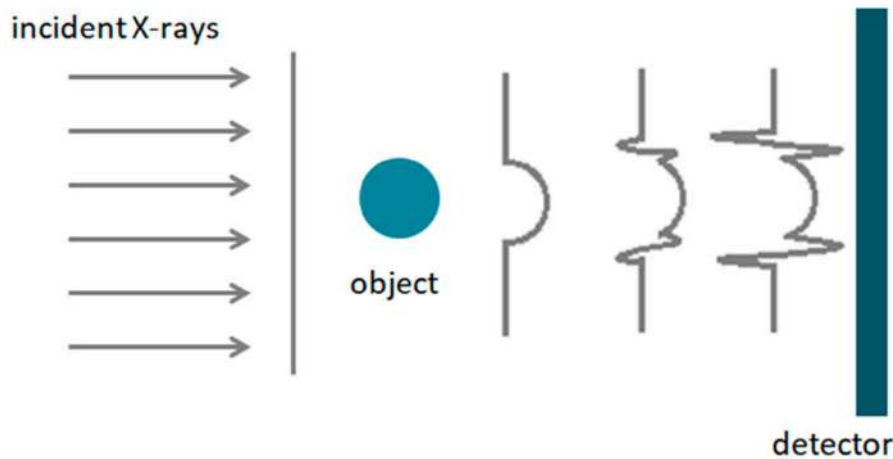


Figure 1.2: Sketch showing the basic principle of propagation-based phase-contrast experiment [5]

because of the interaction of wavefronts that have been phase shifted when propagating inside the sample.

This particular method requires the simplest equipment of all in the phase-contrast family, as it is only needed the X-ray source, the sample, and the detector. As the sketch in Fig. 1.2 shows, the sample is flooded with a parallel X-ray beam that changes the shape of its wavefront because of the phase shift gained after propagating through the material. This modified shape of the wavefront will give rise to constructive and destructive interference that will show fringes in the measured intensity at the detector as a result, especially when there is an abrupt change in the wavefront. This method leads to strong contrast outlining the surfaces and structural boundaries. Then, when combined with CT, the reconstruction of the volume of the sample will show whatever cavities and holes the sample has in its interior.

With the propagation phase-contrast data, one could use diverse phase retrieval algorithms to decode the phase shifts from the intensity patterns collected at a single distance and build a more detailed reconstruction, as in [4].

### 1.3 X-ray diffraction CT

X-ray diffraction Computed Tomography (XRD-CT) complements conventional X-ray CT and offers information on structural parameters (chemical composition and orientation)[2]. This technique relies on information obtained from diffracted rays, rather than attenuated or phase-shifted beams. It has played a major role in the characterization of a wide range of materials since it can provide information on material composition and crystal lattice parameters in bulk materials, without destructive preparation either cutting or powdering [6]. For instance, XRD-CT has been used to reconstruct biological samples (as the study of hydroxyapatite in fossil bones [7]) and inorganic materials (for instance; shale [8]).

To obtain images by diffraction tomography (XRD-CT), a sample is irradiated with a highly collimated, monochromatic X-ray beam and 2D diffraction patterns are collected at an area detector behind the sample. Fig. 1.3 shows the experimental set up for these measurements. The sample is translated along the  $x$  and  $y$  laboratory coordinates so that

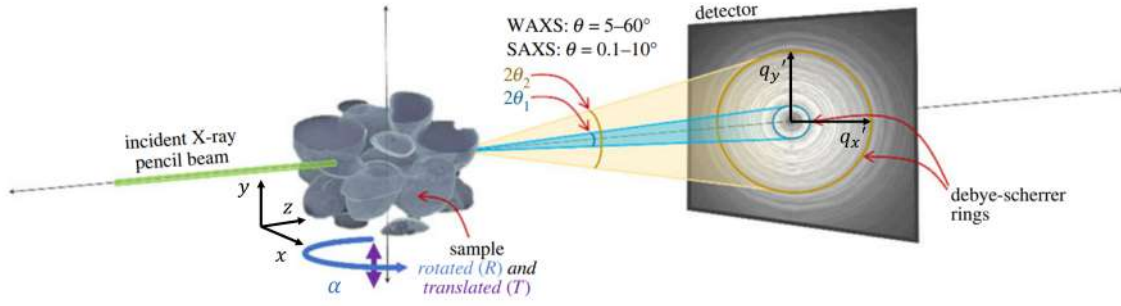


Figure 1.3: Typical set up for XRD-CT experiment [2].

the diffraction pattern is recorded in a screen detector perpendicular to the direction of the pencil beam,  $z$ . Since the diffracted intensity has shape of rings, an azimuthal integration can be performed on the recorded intensity to get  $I(q')$ , where  $q' = \sqrt{q_x'^2 + q_y'^2}$ . Then, the final data set for the XRD-CT reconstruction has the form  $I(x, y, \alpha, q')$ , this is the intensity at a (reciprocal) distance  $q'$  of the center of the detector for every position  $(x, y)$  of the incident beam in the laboratory coordinate system and each orientation  $\alpha$  of the sample around the tomographic axis.

With suitable data processing of these diffraction images, the sample may be reconstructed computationally. This is done with reconstruction algorithms that later will be explained for the specific technique used in this work.

Since synchrotron sources provide high energy X-rays, with much smaller wavelength  $\lambda$  than those experiments with X-ray tubes, from Bragg's law

$$n\lambda = 2d \sin \theta, \quad (1.4)$$

where  $n$  is the diffraction order and  $\theta$  half of the diffraction angle, we see that the angles measured are smaller if one wants to resolve the same features with spacing  $d$ .

The characteristic size of the structure that is to be identified is inversely proportional to the scattering angle, by modifying the distance from the sample to the detector, different scattering angles can be studied. Wide-angle X-ray scattering (WAXS) corresponds to observe scattered angles in the range  $5 - 60^\circ$  and small-angle X-ray scattering (SAXS),  $0.1 - 10^\circ$ , which correspond to resolving nanoscale structures. SAXS imaging has been used for instance to give insight into the evolution of biomineralization processes as precipitation kinetics of  $\text{CaCO}_3$  in [9]. These techniques can be combined with CT to give a full volume reconstruction.

The scattered angle covered by the detector is what determines the range of scale resolution. Depending on what is the scale of structural characteristics that one is interested in in a specific experiment, one method or another can be chosen. Nevertheless, nowadays several set-ups can measure in both ranges of angles being a great tool to study hierarchical materials whose properties depend on their structure at different scales.

## 1.4 X-ray diffraction TT

X-ray diffraction Tensor Tomography (XRD-TT) is an extension of the XRD-CT technique that allows for the study of nanostructure orientation. The experimental set up is similar

to the one of XRD-CT (Fig. 1.3) but, for a more robust reconstruction, projections are often obtained using multiple tomography axes, achieved by using multi-axis stage, see Fig 1.4.

The objective of XRD-TT is to reconstruct the scattering tensor for each voxel in the sample instead of reconstructing a scalar value as it is frequent in conventional CT reconstructions. This way, the structural orientation of every voxel can be obtained.

It is the beam size (area), the scanning step size and the angular spacing between the collected diffraction patterns that determine the spatial resolution in Tensor Tomography. The last two parameters can be tweaked so that resolution is only limited by the size of the X-ray beam, but with the major drawback of increasing scanning time by a large amount, as it is proportional to the fourth power of the number of voxels.

Taking into account the two tomographic axis, all of the measured quantities will be functions of the sample coordinates,  $\mathbf{r}' = (x', y', z')$ , defining the position of the scattering voxel and the reciprocal-space map coordinates,  $\mathbf{q}' = (q'_x, q'_y, q'_z)$ . The real-space position of the voxels can also be expressed in spherical coordinates;  $\mathbf{r}' = (r', \theta', \varphi')$ , where  $\theta'$  is the polar angle and  $\varphi'$  is the azimuthal angle. Then the scattering intensity of every voxel will be  $I(\mathbf{r}', \mathbf{q}')$ , which is a six-dimensional quantity that gives more information for orientational reconstruction in contrast to the typical five-dimensional quantity that can be obtained with a single tomography axis,  $I(x, y, \alpha, q_x, q_y)$ , described in Section 1.3.

Measurements for this reconstructions are diffraction patterns for each  $(x, y, \phi, \chi)$ , a particular incident position of the beam (in laboratory coordinates) and sample orientation. As in traditional XRD-CT, these diffraction patterns contain information on the crystal structure since the registered intensity distribution  $I(\mathbf{q})$  is proportional to the absolute square of the Fourier Transform of the electron density distribution. In the case when the scattering is not isotropic, showed as variation of  $I$  with the detector azimuthal angle  $\varphi$ , the patterns also contain information on the orientation of the diffracting crystals.

The objective of the reconstruction is to determine a 3D reciprocal-space map,  $\hat{R}(\mathbf{r}', \mathbf{q}')$ , that models the scattering from every voxel in the sample. This map is going to be

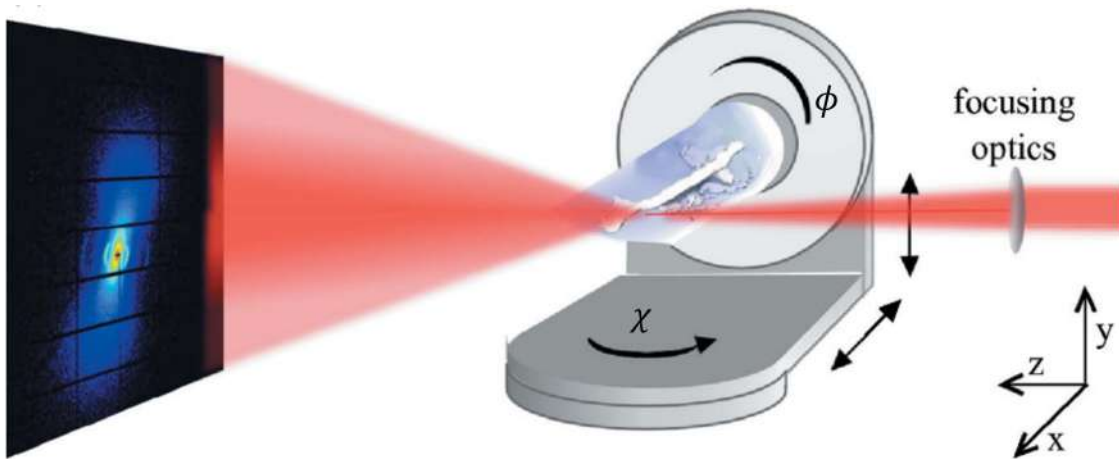


Figure 1.4: Typical set up for XRD-TT experiment [10].

constructed using spherical harmonic functions  $Y_l^m$  as the basis,

$$\hat{R}(\mathbf{r}', \mathbf{q}') = \left| \sum_{l,m} a_l^m(\mathbf{r}', q') Y_l^m[\Theta(\mathbf{r}', q'), \Phi(\mathbf{r}', q')] \right|^2, \quad (1.5)$$

where  $a_l^m(\mathbf{r}', q')$  are the weighting coefficients and  $\Theta(\mathbf{r}', q')$  and  $\Phi(\mathbf{r}', q')$  are the polar and azimuthal angle arguments for the spherical harmonic functions with respect to the sample coordinates.

Each voxel has a preferred orientation given by the unit vector  $\hat{\mathbf{u}}_{\theta_{op}, \varphi_{op}}^{str}(\mathbf{r}', q')$  which is parameterized by the angles  $\theta_{op}(\mathbf{r}', q')$  and  $\varphi_{op}(\mathbf{r}', q')$ . The relation between the angle arguments of the spherical harmonics and the liked orientation per voxel is

$$\begin{pmatrix} \sin \Theta \cos \Phi \\ \sin \Theta \sin \Phi \\ \cos \Theta \end{pmatrix} = \begin{pmatrix} \cos \theta_{op} \cos \varphi_{op} & \cos \theta_{op} \sin \varphi_{op} & -\sin \theta_{op} \\ -\sin \varphi_{op} & \cos \varphi_{op} & 0 \\ \sin \theta_{op} \cos \varphi_{op} & \sin \theta_{op} \sin \varphi_{op} & \cos \theta_{op} \end{pmatrix} \times \begin{pmatrix} \sin \theta' \cos \varphi' \\ \sin \theta' \sin \varphi' \\ \cos \theta' \end{pmatrix}. \quad (1.6)$$

It is the parameters  $a_l^m(\mathbf{r}', q')$ ,  $\theta_{op}(\mathbf{r}', q')$ , and  $\varphi_{op}(\mathbf{r}', q')$  that the algorithm for the reconstruction is aimed to find.

As the quantity inside the vertical bars in (1.5) is the scattered amplitude,  $\hat{R}(\mathbf{r}', \mathbf{q}')$  describes the scattering intensity per voxel  $\mathbf{r}'$ , in the position  $\mathbf{q}'$  of the detector. So the total scattering intensity that the model predicts for a specific point in the detector, will be the summation of the scattering intensities per voxel for all of the voxels in the beam path,  $\hat{z}$ , (assuming single scattering events)

$$\hat{I}_n(x, y, \mathbf{q}') = \sum_z \left| \sum_{l,m} a_l^m(\mathbf{r}', q') Y_l^m[\Theta(\mathbf{r}', q'), \Phi(\mathbf{r}', q')] \right|^2, \quad (1.7)$$

which in the plane of the detector,  $\mathbf{q}' = (q_x, q_y, 0)$  or  $(q, \pi/2, \varphi)$ , takes the form

$$\hat{I}_n(x, y, q, \varphi) = \sum_z \left| \sum_{l,m} a_l^m(\mathbf{r}', q') Y_l^m[\Theta(\mathbf{r}', q')|_{\theta=\pi/2}, \Phi(\mathbf{r}', q')|_{\theta=\pi/2}] \right|^2, \quad (1.8)$$

the subscript  $n$  indicates a particular orientation of the sample.

The lowest order spherical harmonic,  $Y_0^0$ , describes isotropic scattering and higher orders can be found to describe more complex scattering patterns. In practice, in our reconstructions we will only use even polar orders ( $l$ ) and up to 6, and the azimuthal order ( $m$ ) will always be 0 (the orientation distributions are assumed to be uniaxial), this is  $l = [0, 2, 4, 6]$  and  $m = [0, 0, 0, 0]$ .

In order to find the right model  $\hat{R}(\mathbf{r}', \mathbf{q}')$  (this is, finding the right  $a_l^m$ ,  $\theta_{op}(\mathbf{r}', q')$  and  $\varphi_{op}(\mathbf{r}', q')$  parameters, which describe the preferred orientation direction in each sample voxel) that correctly describes the scattering intensity measured at the detector  $I_n(q_x, q_y) = I_n(q, \varphi)$ , the cost function

$$\varepsilon_q = 2 \sum_{n,x,y,\varphi} \omega_n(x, y, q, \varphi) \left\{ [\hat{I}_n(x, y, q, \varphi)]^{1/2} - \left[ \frac{I_n(x, y, q, \varphi)}{T_n(x, y)} \right]^{1/2} \right\}^2 \quad (1.9)$$

has to be minimized (through a gradient-based method[10]). Here  $T_n(x, y)$  is the transmitted intensity at each point and  $\omega_n(x, y, q, \varphi)$  is a binary mask used to define the valid data regions (1) and the invalid data regions (0).

The reconstruction algorithm starts by optimizing the coefficients that describe the symmetric scattering intensity,  $a_0^0(\mathbf{r}', q')$ . Then, a 3D mask ( $\omega$ ) for the voxels that are not going to be optimized is created. Next step is to optimize the spherical harmonic angles  $\Theta(\mathbf{r}', q')$ , and  $\Phi(\mathbf{r}', q')$  for the orientation of every voxel. Finally, the coefficients describing the non symmetric scattering are found,  $a_l^m(\mathbf{r}', q')$ , with  $l = [2, 4, 6]$  and  $m = [0, 0, 0]$ . The reason for keeping the azimuthal order to be null is that the crystallites are assumed to be distributed randomly about their long axis, what results in uniaxially symmetric intensity distributions. The periodicity of scattering properties of electrons in XRD patterns allow us to restrict the polar order to even numbers.

A way of measuring average orientation over a region of space is using the Hermans' orientation parameter

$$S = \frac{1}{2}(3\langle \cos^2 \Theta \rangle - 1), \quad (1.10)$$

that takes values from -0.5 to 1, which extremes correspond to total orientation along  $\Theta = 90^\circ$  and  $\Theta = 0^\circ$ , respectively, and  $S = 0$  describes isotropic samples (no degree of orientation at all)[11].

In this work we have tested XRD-Tensor Tomography by reconstructing the volume of a gallbladder stone using the algorithm described previously.

## Chapter 2

# Materials and Methods

### 2.1 Gallbladder stones

Gallbladder stones (or simply gallstones) are small hardened deposits of bile (digestive fluid) stored in the gallbladder organ. They represent a form of pathological biomineralization. Usually, gallstones are made of cholesterol crystals, more precisely of cholesterol monohydrate crystals, or calcium bilirubinate (the so-called pigment stones) and do not represent any health threat as they do not give life to any symptom. But if these stones are thrown out into a duct and it is blocked, they may cause cramping pain.

Cholesterol is a type of lipid present in different body tissues. It is synthesized by all animal cells and it serves as a precursor for the biosynthesis of bile acid [12]. Indeed, the word *cholesterol* comes from the Greek root *chole*, which means "bile", and *steros*, "solid" [13]. In particular, the stone we are using as a sample in this experiment is formed of cholesterol monohydrate crystals (CMH) -we will show this later by studying the diffraction peaks- which are cholesterol crystals that contain one molecule of water ( $\text{H}_2\text{O}$ ) per cholesterol molecule ( $\text{C}_{27}\text{H}_{46}\text{O}$ ). The structure of both, the cholesterol monohydrate molecule and cholesterol monohydrate crystal can be seen in Fig. 2.1. In particular, Fig. 2.1b shows how CMH crystals have a long axis, it is the periodicity along this long axis that gives rise to the strong Bragg peaks that are measured.

There are occasions in which accurate visualization of the studied object is needed for delivering optimal and precise results. In these circumstances, CT is preferred above traditional X-ray scans as this technique offers a much more faithful and reliable representation of objects than the planar radiographic projections that do not preserve the true geometry of the studied sample. This is a non-negotiable trait in a lot of biological applications.

This is why it is of interest to use CT scans on gallstones, not only for their detection in human beings (with abdominal CT, in a hospital installation) but also for the structural study of these stones. Learning how gallbladder stones are created and their evolution over time are key parameters for defining and implementing an effective medical treatment [16].

The microstructural nucleation events that lead to the creation of the stones, remain less understood. It is true that the cholesterol monohydrate orientation within the gallstones can be studied using traditional microscopy techniques as polarised microscopy, but these



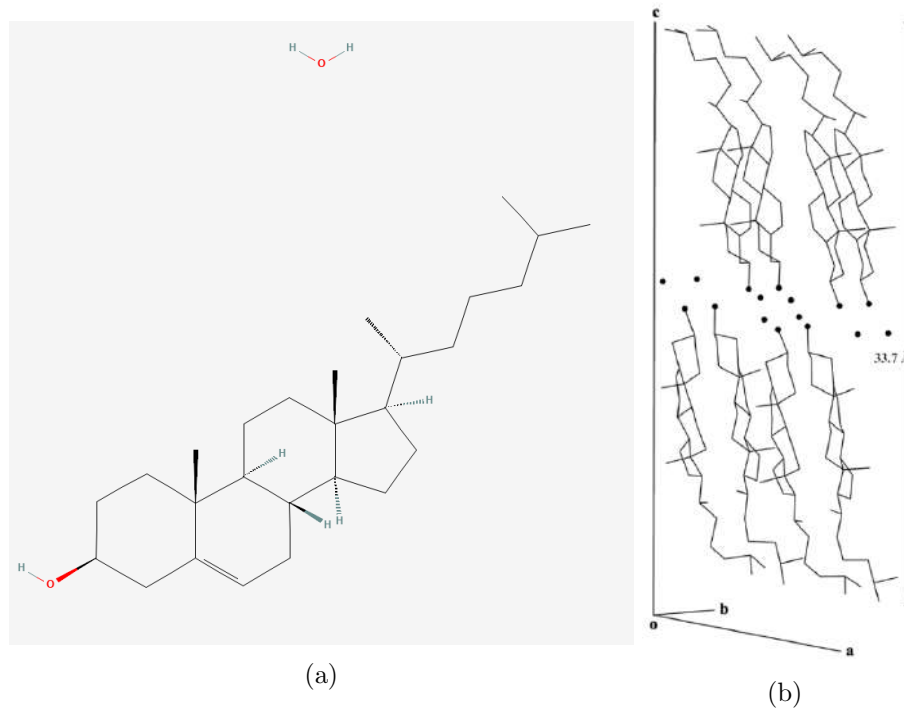


Figure 2.1: (a) 2D structure of cholesterol monohydrate molecule ( $\text{H}_2\text{O} + \text{C}_{27}\text{H}_{46}\text{O}$ ) [14]. (b) Bilayer crystalline structure of cholesterol monohydrate showing the distance between planes in the 001 family set. Dark atoms represent oxygen. [15].

involves sectioning of the sample in thin slices, and then it would be destroyed and potentially changed its structure. XRD-CT is sensitive to the chemical content of the sample, which is difficult to be probed by  $\mu$ -CT as it relies on contrast due to absorption. Even though both techniques have similar resolution, conventional CT cannot show the orientation distribution over large distances ( $\sim \mu\text{m}$ ), even if it could resolve individual crystallites. This is where XRD-TT comes in, providing the necessary orientational contrast to study the cholesterol monohydrate crystallites in gallstones.[17] [7].

## 2.2 Experimental setup and parameters

A schematic diagram of the experimental setup for both PPC-CT and XRD-TT measurements can be seen in Fig. 1.1b and 1.4, respectively. The measurements for both experiments were collected in February 2022 at ID15A beamline at the European Synchrotron Radiation Facility (ESRF) in Grenoble, France.

### PPC-CT measurements

The PPC-CT measurements were taken with a PCO EDGE hs detector that has a pixel size of  $6.5 \mu\text{m}^2$  and  $2560 \times 2160$  pixels that correspond to a sensitive area of  $16.64 \times 14.04 \text{ mm}^2$ . The exposure time for every measurement was of 0.01 s.

3100 different projections (as the one in Fig. 2.2a) were taken on 9 different zones of the sample (this is a total of 27900 scans), in a range of  $185^\circ$ , what corresponds to an angle step of  $0.06^\circ$ . But these projections have two sources of errors that can be removed by subtracting two new measurement; stray light and electronic noise. So, after scanning each



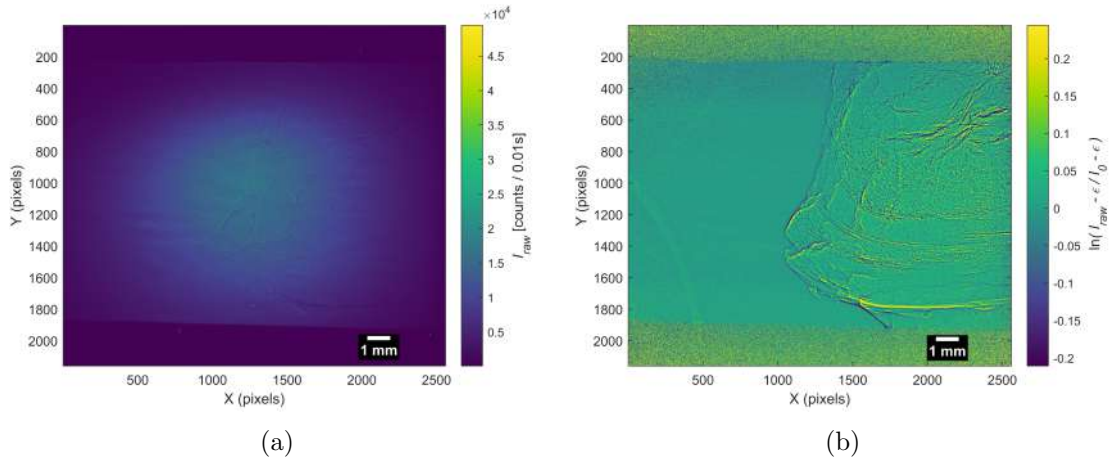


Figure 2.2: (a) Projection for a particular zone and orientation of the sample ( $\alpha = 0^\circ$ ). Colormap indicate number of counts in every pixel in the exposure time. (b) Same projection corrected with the bright mean and electronic noise measurements and processed to display the negative of the optical density,  $OD$ .

zone in the sample two more measurements were taken, one without the sample to account for a white reference (flat field) and one covering the detector to account for electronic noise.

With these measurements, a correction to the projections and processing to obtain the optical density was performed and using Beer-Lambert's law

$$-OD(x, y) = \ln \left( \frac{I_{\text{raw}}(x, y) - \epsilon(x, y)}{I_0(x, y) - \epsilon(x, y)} \right), \quad (2.1)$$

where  $I_{\text{raw}}$  refers to the number of counts in the raw measurement (Fig. 2.2a),  $I_0$  to the flat field measurement, and  $\epsilon$  is the measurement for the electronic noise, a map of the optical density of the sample can be obtained.

The result of normalizing and taking the logarithm of the intensity yields the negative of the optical density,  $-OD$ . In the context of phase-contrast imaging, this value is related to the phase shift induced by the sample. Specifically, for weak phase objects,  $OD$  is proportional to  $(k\delta t)^2$ , where  $k$  is the wavenumber of the X-ray,  $\delta$  is the refractive index decrement, and  $t$  is the thickness of the sample that the X-ray traverses.

This processing enhances the visibility of phase-related contrast data, effectively highlighting the phase changes that the X-rays undergo when passing through the sample. The resulting processed image, which emphasizes phase contrast, can be seen in Fig. 2.2b.

## XRD-TT measurements

The diffraction patterns for the XRD-TT reconstruction were taken with Pilatus3 X detector, which has a sensitive area of  $253.7 \times 288.8 \text{ mm}^2$  with  $1475 \times 1697$  pixels which translates to a pixel size of  $0.172 \times 0.172 \text{ mm}^2$ . This detector has a hybrid pixel technology; first of all, X-rays are converted into electric charge in the sensor pixel and then, the electric signal is processed and counted in the readout pixel, see Fig. 2.3. This signal has to be above a threshold so the count is effectively made so that dark current noise is

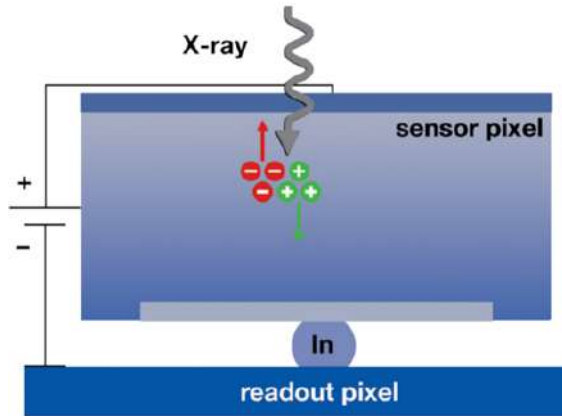


Figure 2.3: Hybrid pixel detector in Pilatus3 X 2M [18].

abolished. Both are connected in such a way that there is no possible spread or loss of signal [18].

The X-ray pencil beam used in the collection of the data was shaped with  $25 \times 25 \mu\text{m}^2$  size and it was characterised by a wavelength of  $\lambda = 0.2480 \text{ \AA}$ , which corresponds to an energy of  $E = 50.00 \text{ keV}$ . The exposure time for every pattern was of  $0.10 \text{ ms}$  and the sample-detector distance in this set-up was  $2402 \text{ mm}$ , which means that we are looking at a range  $2\theta = 0.1^\circ - 3.5^\circ$  of the scattering angle. Using Bragg's law, Eq. 1.4, with the distance between [001] planes displayed in Fig. 2.1b,  $33.7 \text{ \AA}^{-1}$ , one can calculate that this family of planes will scatter the  $E = 50.00 \text{ keV}$  X-rays with an angle  $2\theta = 0.42^\circ$ .

For each particular orientation of the sample, given the two tomographic angles,  $\chi$  and  $\phi$ , (this is to create a single projection) 10285 diffraction patterns were taken, each with a different incidence position of the beam ( $\sim 100$  steps in each direction), sweeping all of the sample. The step size was  $0.025 \text{ mm}$ , so the total swept area is of  $2.5 \times 2.5 \text{ mm}^2$ . The angular step size for one of the tomographic angles ( $\chi$ ) was of  $5^\circ$  from  $0^\circ$  to  $40^\circ$ . In the other angular direction ( $\phi$ ), the step size is not the same for every value of  $\chi$ , but it increases with increasing values of  $\chi$ . For instance, the angular step size in  $\phi$  direction for  $\chi = 0^\circ$  it is of  $2.25^\circ$  and for  $\chi = 40^\circ$  it is of  $18^\circ$ .

Fig. 2.4 shows a diffraction pattern collected for the XRD-TT reconstruction. This pattern displays various Bragg peaks for the cholesterol monohydrate crystal, with the 001 peak highlighted. This particular peak will be utilized in forming the projections.

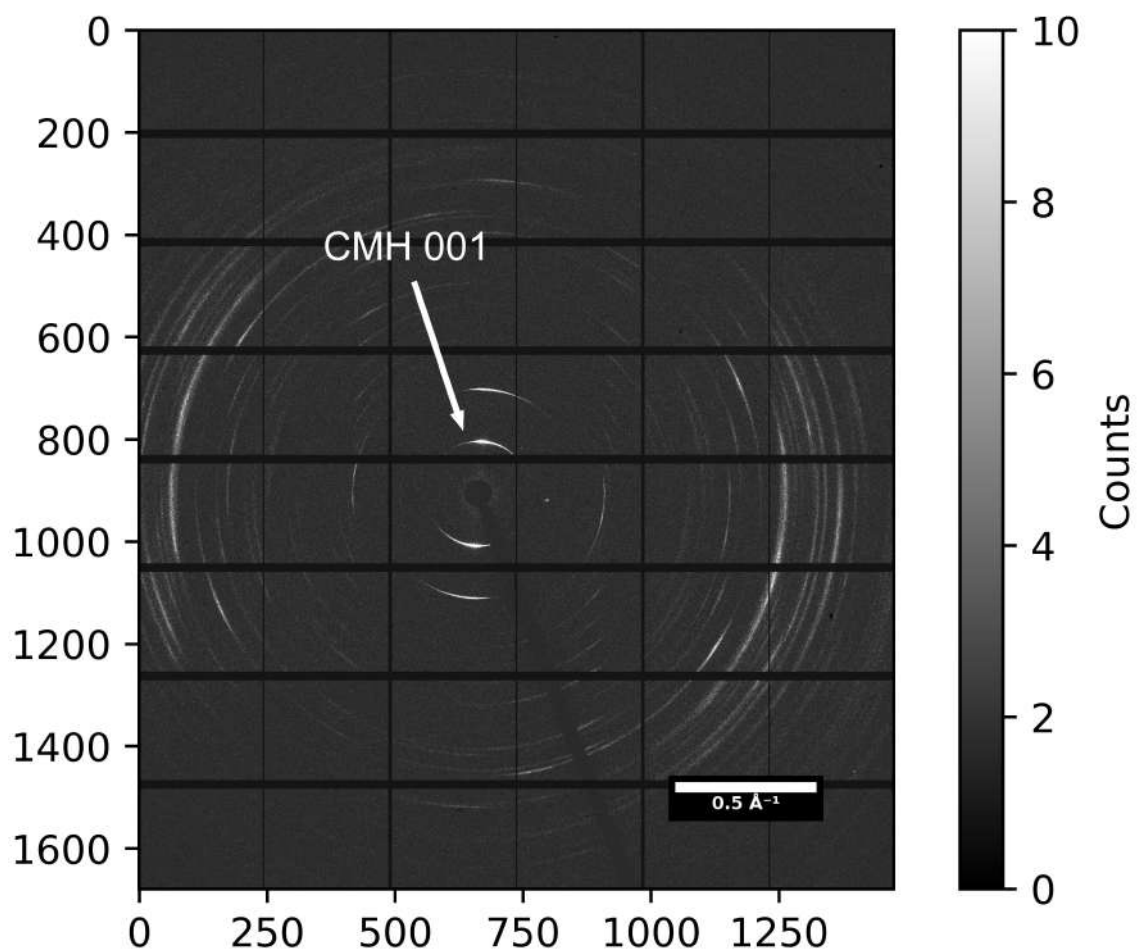


Figure 2.4: Example of a collected diffraction patterns used in the XRD-TT reconstruction. Color scale indicates number of counts in each pixel. The beam stop support can be seen as a dark line in the bottom right zone and the 001 Bragg peak for cholesterol monohydrate (CMH) crystal is pointed with an arrow.

## Chapter 3

# Results and Discussion

The purpose of this study is to test the XRD-TT reconstruction technique with the algorithm described previously on a gallstone sample. This reconstruction will provide us with information about the orientation distribution of the cholesterol monohydrate crystals that make up the stone. To understand how this orientation relates to the structure of the sample, including surfaces, boundaries, and internal cavities, we will compare the Tensor Tomography reconstruction with a typical Computed Tomography reconstruction, specifically a propagation phase contrast CT. This comparison will also help us evaluate the validity of the TT reconstruction in terms of volume size and shape.

### 3.1 PPC-CT reconstruction

#### Projections

From the measurements and the correction discussed in Section 2.2 and shown in Fig. 2.2, we can get a full set of projections of the stone by stitching the different areas that the measurements were taken at. Some of these projections can be seen in 3.1. Because the X-ray source has an intensity fluctuation over time not all of the corrections have the same values for the background. This variation is evident in the stitched projections, as each area displays a different background color. In the end, this will have an impact on the quality of the final reconstruction.

#### Reconstruction

To reconstruct the volume of the sample from the set of propagation phase contrast projections, we have used the *TomoPy* package for Python [19] combined with the *Astra* toolbox [20]. In particular, the reconstruction has been performed with the Filtered Back Projection (FBP) method.

The reconstruction result from using a low number of projections (only 1 every 10) from the complete set and using half of them is shown in Fig. 3.2a. We can see that in the reconstruction that uses more projections, the resolution is better, allowing us to identify smaller features (such as the cavities inside the sample), than in the first reconstruction. Also, the size of the reconstruction is bigger (includes more voxels), then, there are many more slices to observe in a better way the little details.

It is interesting to see that there is an improvement in the quality of the reconstruction not

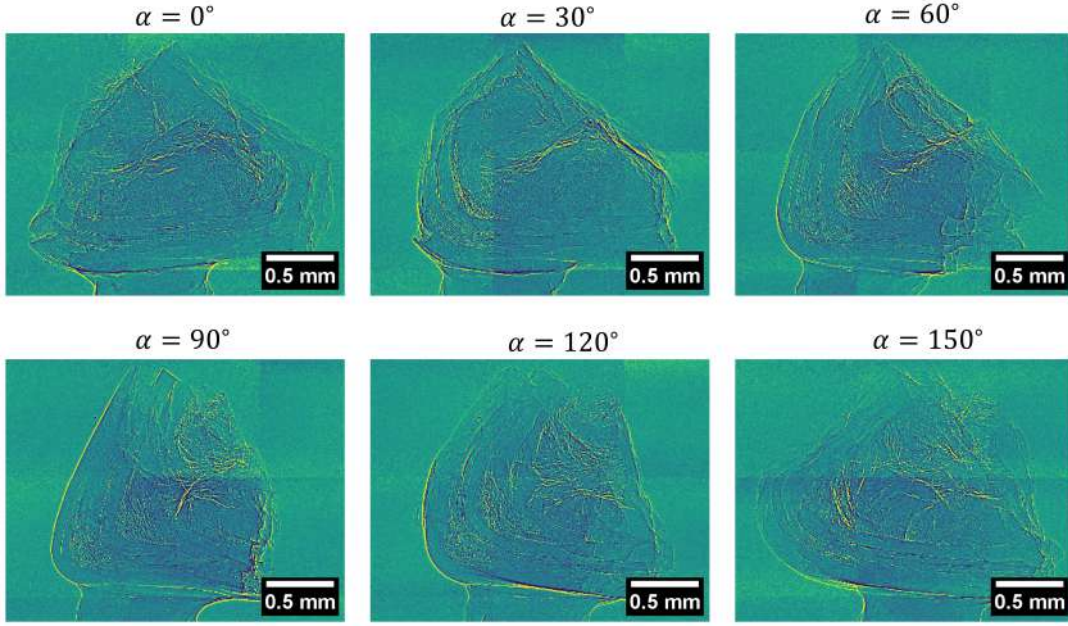


Figure 3.1: Stitched and corrected projections for different angles  $\alpha$  around the tomographic axis.

only in the resolution but also when it comes to the artefacts. Artefacts are an inherited trait of any CT reconstruction since they appear due to the lack of idealised conditions such as not having enough photon counts, not using monochromatic X-rays, lack of infinite detector resolution that prevent us from having an image that reflects all of the features of the sample in the best possible way [21]. Nonetheless, the contribution of these to artefacts in our reconstruction is negligible since the imperfections that can be seen in Fig. 3.2a are due to not having found the best possible center of rotation for the reconstruction and the imperfect stitching of the projections.

We can see in the reconstruction that uses fewer amount of projections that there seem to be some lines that propagate across the slice on the edge of the sample. When using more projections, these lines seem to diminish and only appear where there are big changes in the reconstruction values. This is a common effect in CT reconstructions when undersampling a projection or using too small number of views [1].

Nevertheless, the PPC-CT reconstruction has provided high-resolution insights into the shape and internal morphology of the gallstone, showing holes and cavities. This type of inside cracks that are in the reconstructed gallstone, as well as the layered structure that can be seen close to the edges of the stone, also show up in other samples, as it was reported in the reconstruction of other gallstones in [16]. Additionally, the brighter spots in the central cavities might indicate that the stones are formed through a process of nucleation and growth.

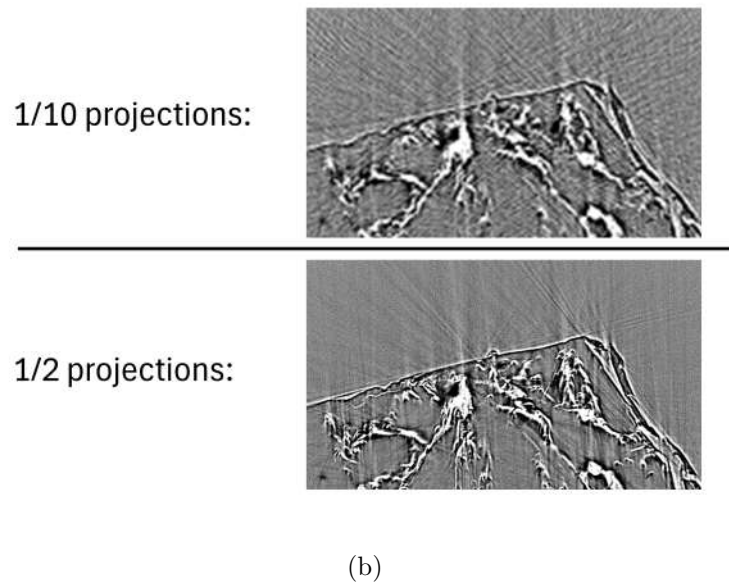
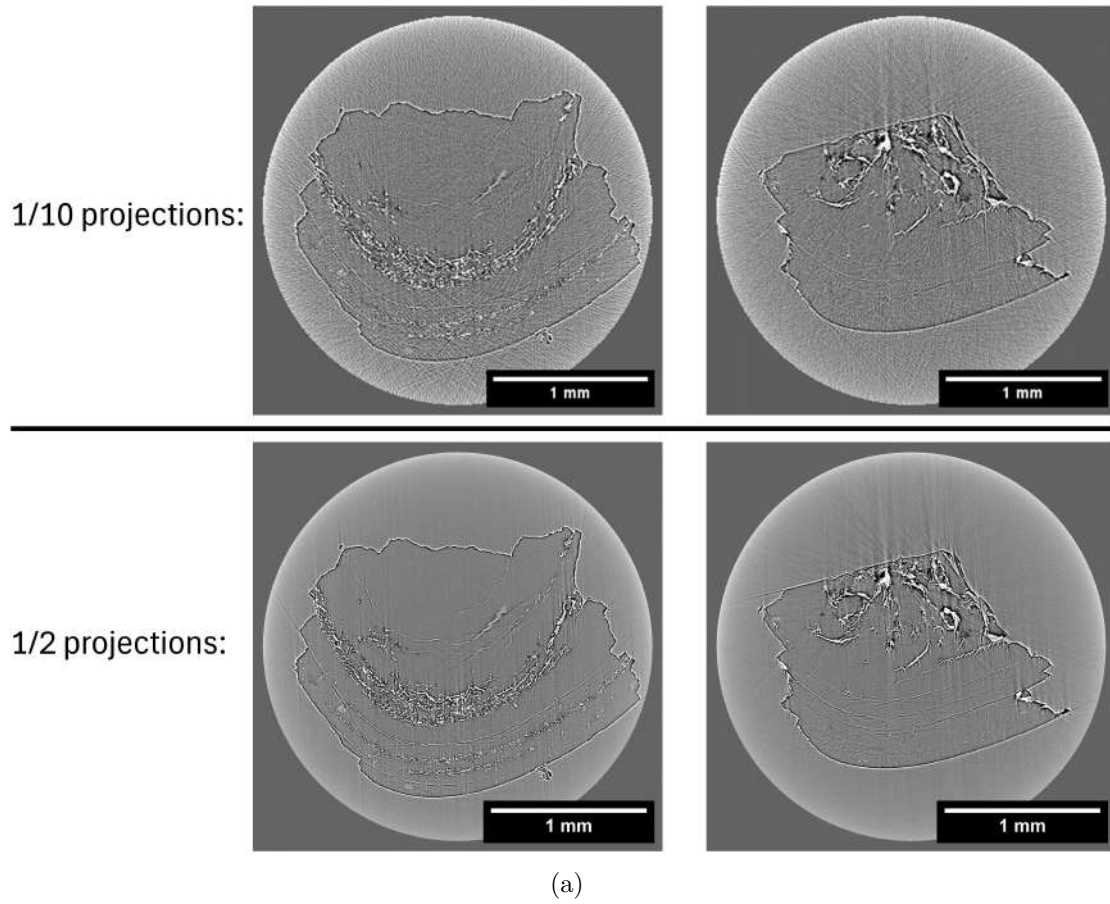


Figure 3.2: (a) Comparison of two different slices in the reconstructed volume for different amount of PPC projections used. (b) Zoomed section in the slice on the right side for both reconstructions.

## 3.2 XRD-TT reconstruction

### Projections

By azimuthally integrating all of the diffraction patterns for a particular orientation of the sample, it is possible to obtain a plot of the radial distribution of the intensity in reciprocal space,  $I(q)$ , as the one in Fig. 3.3a. This plot allows us to identify the different Bragg peaks in the diffraction patterns and determine which crystalline materials make up the gallstone. Fig. 3.3a shows that the first Bragg peak, 001, is the most prominent. Based on this diffractogram, we can conclude that the gallstone is formed of cholesterol monohydrate crystals by comparing it to diffraction peaks that other gallbladder stones exhibit, [15], see Fig. 3.3b, which have been identified to be samples formed completely by cholesterol monohydrate crystals, and seeing how Bragg peaks appear at the same reciprocal positions,  $q$ .

Integrating in the range of  $q$  in which the first Bragg peak lies and merging the result for all of the measured patterns for a specific orientation of the sample (fixed  $\chi$  and  $\phi$ ), we can build projections as shown in Fig. 3.4 that show the scattering intensity of the crystals and already give an insight into the shape of the stone.

It is interesting to notice how both, the projections for the XRD-TT measurements and the projections for the PPC-CT measurements show similar shapes if compared as in Fig. 3.5. This indicates that the study of the diffraction patterns, its azimuthal integration, and the construction of the projections was done in a correct way.

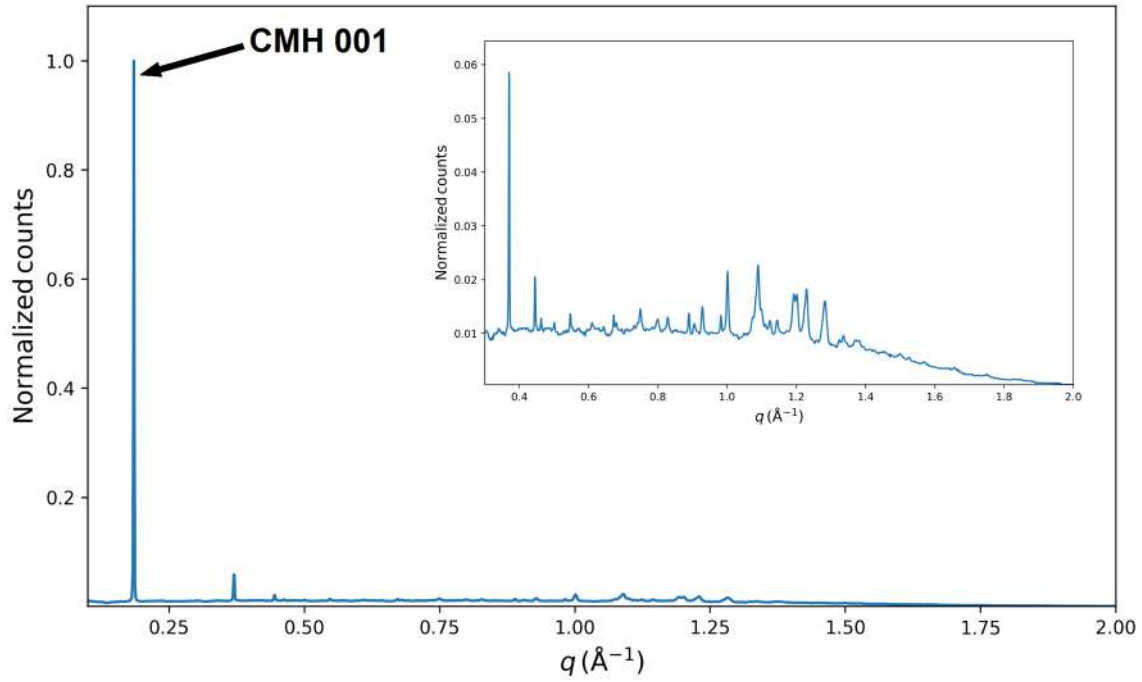
### Reconstruction

The algorithm described in Section 1.4 was implemented as a **MATLAB** routine by the CSX group at the Paul Scherrer Institut (PSI) [22]. First of all, from the projections, the coefficients that describe the symmetric scattering  $a_0$  are optimized. Then, it is the preferred orientation of every voxel (given by  $\theta_{op}$  and  $\phi_{op}$ ) that is optimized which is related to the spherical harmonic argument angles,  $\Phi$  and  $\Theta$ , by Eq. 1.6. In the end, the rest of the coefficients  $a_l^m$  are optimized. Here, it is only included those of even polar order,  $l$ , up to 6 and of 0 azimuthal order,  $m$ . The  $m = 0$  constriction assumes that the crystallites are distributed randomly about their long-axis giving uniaxially symmetric intensity distributions. The restriction that keeps the spherical harmonic function with  $l$  even is justified due to the scattering properties of periodic electronic structures valid in XRD patterns.

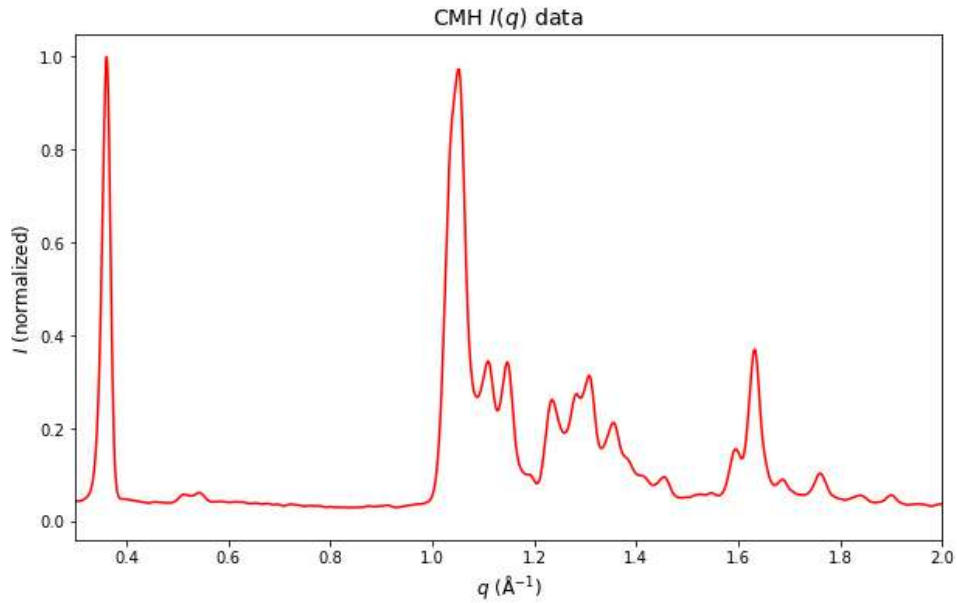
For a better visualization of the result, it is interesting to only show a portion of the voxels in a thin slice, orthogonal to three directions as it is shown in Fig. 3.6a. We see that the two slices displayed in the upper part of Fig. 3.6a reproduce the shape of the stone in the phase-contrast projections (see Fig. 3.1) for  $\alpha = 0^\circ$  and  $\alpha = 90^\circ$ . Also, the reconstruction reveals that there is a tendency for cholesterol monohydrate crystals to orient themselves with their long axis parallel to the sample edges, and how the orientation changes to be more varying in the center as the zoomed regions in Fig. 3.6b show.

This reconstruction was made using half of all of the available projections, but another one was done before using only 1/15 projections. A comparison between these two can be seen in Fig. 3.7, where again, three central slices, orthogonal to the same three directions as in Fig. 3.6a, is shown. In the second reconstruction, it is visible how the stone shows





(a)



(b)

Figure 3.3: (a) Diffractogram obtained by adding all of the collected diffraction patterns for a particular orientation of the sample and integrating azimuthally the intensity (counts) of X-rays. The most prominent Bragg peak (001) is marked as it is the one that we will be using to integrate the projections and a zoomed version for  $q > 0.3 \text{\AA}^{-1}$  is given. (b) Data from [15] for cholesterol monohydrate gallstones scattered intensity,  $I(q)$ , for  $q > 0.3 \text{\AA}^{-1}$ .



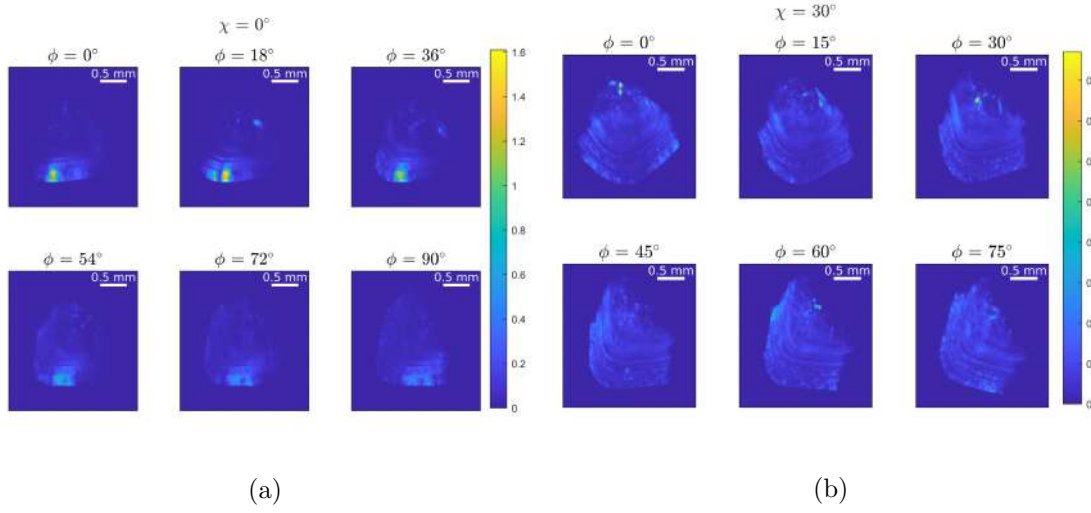


Figure 3.4: Azimuthally integrated projections for the cholesterol monohydrate 001 Bragg peak. Colormap shows intensity of scattering in every zone.

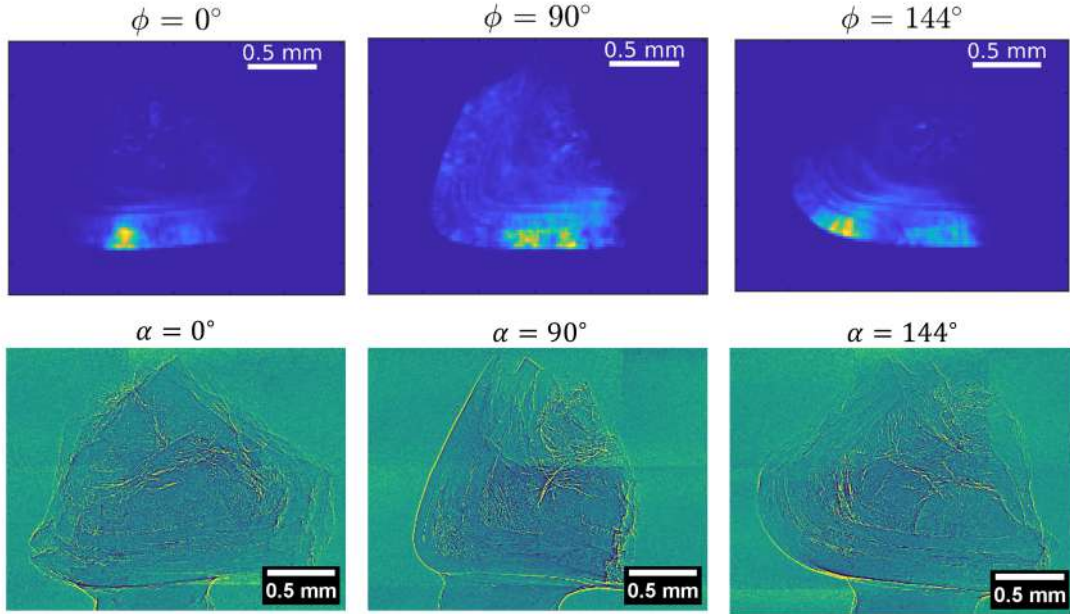


Figure 3.5: Comparison between constructed projections from the diffraction patterns (raw data for XRDTT reconstruction) and stitched and corrected Propagation-based Phase Contrast projections. Three projections are shown for different orientations of the sample around one of the XRDTT tomographic axis, keeping  $\chi = 0^\circ$ . Note that the colorscale showing the intensity of scattering for the XRDTT projections is not global as in 3.4 but different for each projections so the shape shown in each can be appreciated in a better way.

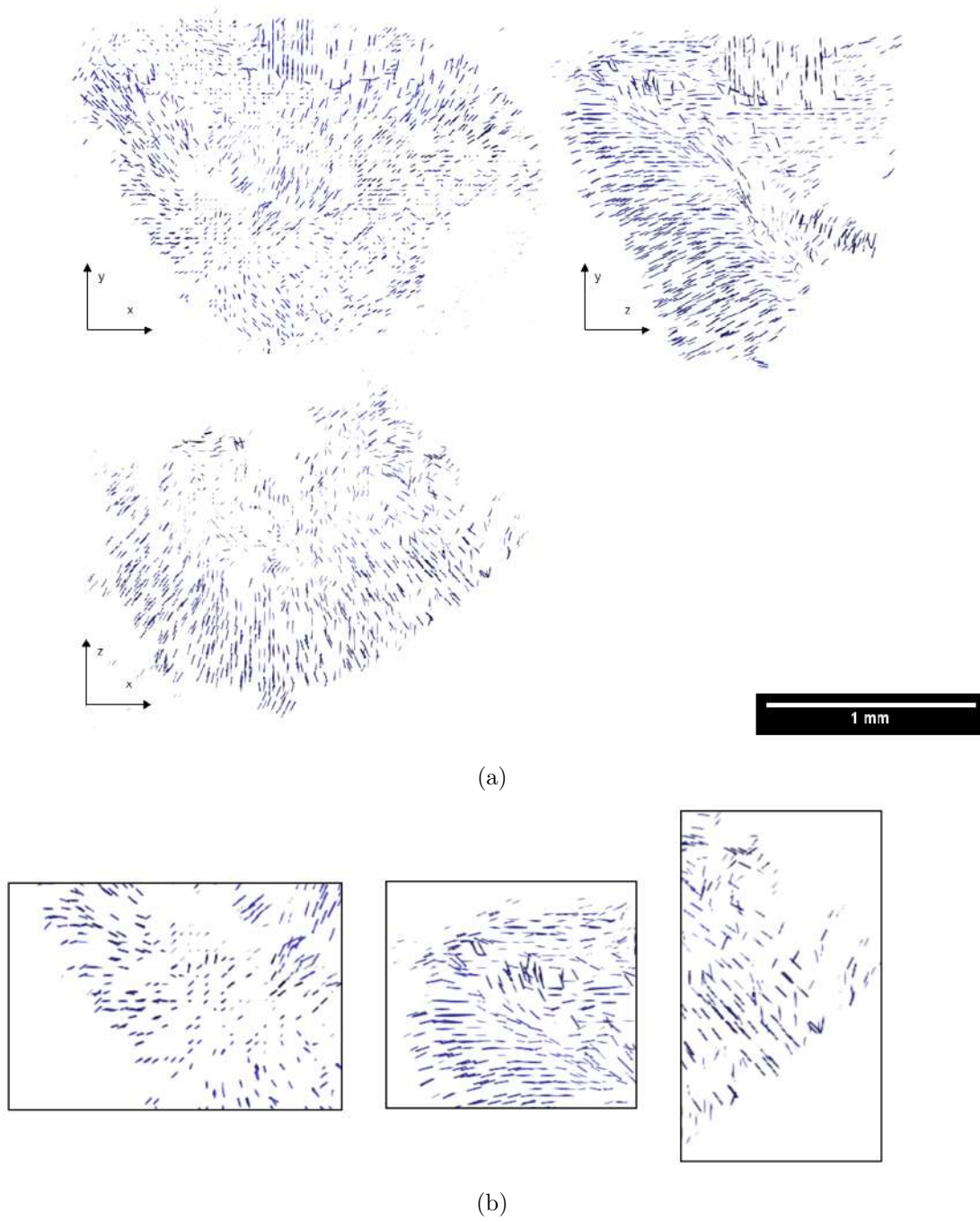


Figure 3.6: (a) Visualization of the orientation of the scattering voxels in the three dimensional XRDTT reconstruction. Only orientation of voxels in 3 thin perpendicular slices from approximately the center of the sample are plotted. (b) Zoomed view of different parts of the 3 slices.

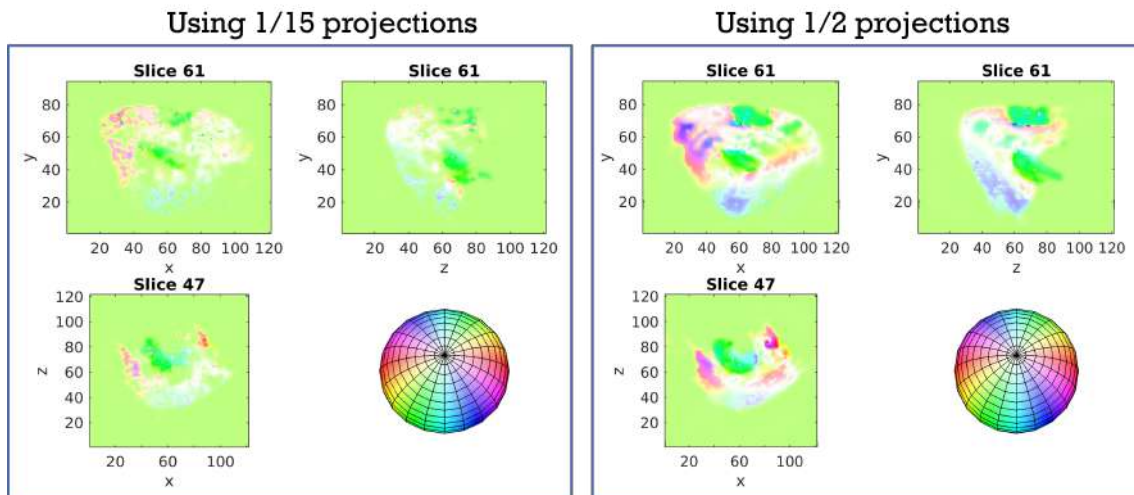


Figure 3.7: Reconstruction of gallstone from spherical harmonics scattering map using 1 every 15 projections and using half of the projections. Views are for three perpendicular slices from approximately the center of the sample (same as in Fig 3.6a). Colours shows direction of scattering in every area.

and ordered structure and we can recognize which is the general direction of scattering of every area in it. Fig. 3.7 displays again the feature that the orientation of the cholesterol monohydrate crystals is towards the outside around the borders of the stone. One can see how when more projections are used the quality of the reconstruction improves since the the regions with the same direction of scattering are better defined.

By evaluating the azimuthal variations of intensity that show up in the diffraction patterns, we obtained a preliminary idea of how the cholesterol monohydrate crystals are oriented in the outermost layer of the sample. Fig. 3.8 shows this information on top of the reconstructions. This was done only by using Fourier analysis and it is important to note that it does not require any of the techniques mentioned before for Tensor Tomography reconstruction. Also, in this process, it has been assumed that the cholesterol molecules are oriented with their long axis parallel to the scattering direction. Additionally, Fig. 3.8 shows the result of the TT reconstruction over the projections so it can be checked with the just described analysis. We can see how both outcomes match (at least where the scattering direction information is strong enough so that it could be predicted by Fourier analysis) which is a good indication that the reconstruction worked correctly.

In all of the Figures showing the results of the reconstruction (3.6, 3.7, and 3.8) we can see that the stone presents an ordered structure, not with random scattering at every voxel but the crystals are arranged in areas with the same orientation and it does not display sudden changes in space. This is a feature that could be predicted from the measured orientation in Fig. 3.8 but it is also a characteristic that we could expect in this type of sample from the way gallstones are formed. Otherwise, if the reconstruction only showed the same orientation across all of the sample, that would mean that the resolution of the experiment was not good enough. At the same time, if the voxel size was too small, it would be difficult to reconstruct since few crystallites in the voxel volume would give abruptly shaped intensity distributions instead of smooth variations with distance.

The XRD-TT analysis and reconstruction indicate that the gallbladder stone used as sample in this work consists of cholesterol monohydrate crystals. The presence of this

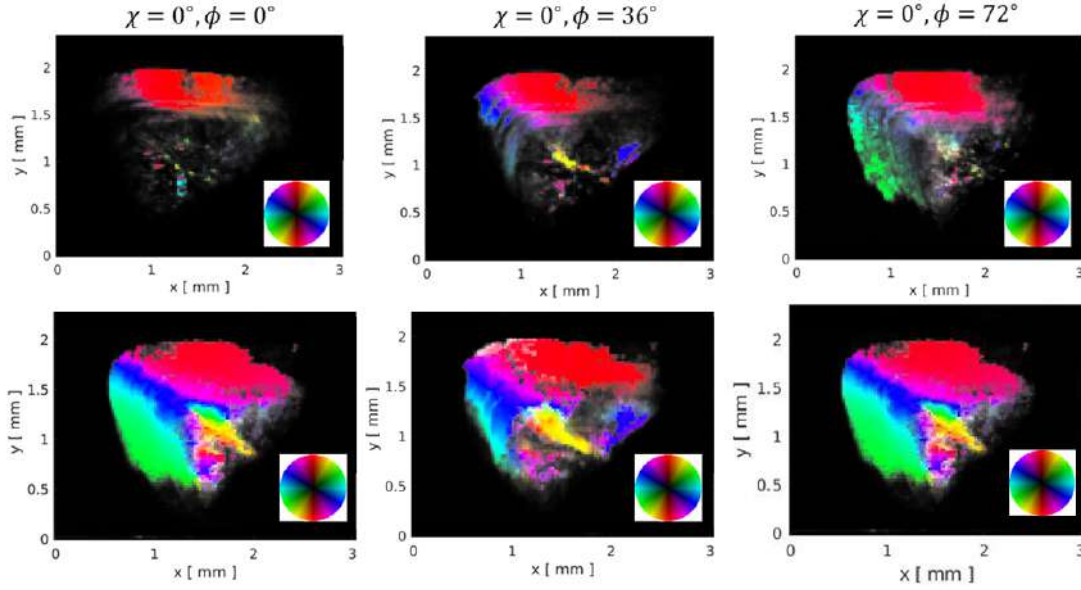


Figure 3.8: On the upper part, measured scattering orientation of the cholesterol monohydrate crystals from Fourier Analysis. On the lower part, simulated scattering orientation. Colorwheel shows the correspondence between colors and direction of scattering.

specific phase aligns with previous phase composition analysis of human gallstones using different techniques such as infrared spectroscopy and scanning electron microscopy [15]. Additionally, we were able to find that this crystallites that form up the gallstone exhibit a preferred orientation that is towards the outside in the borders of the sample and varying in different regions of the sample. The preferred orientation suggests that crystallization occurs under specific physiological conditions that give rise to the patterns in Fig. 3.6.

### Comparison of PPC-CT and XRD-TT reconstructed cross-sections

In our previous discussion (refer to Fig. 3.5), we established that the stitched projections for the Propagation Phase-Contrast data and the integrated projections from the diffraction patterns accurately depict the sample's shape, indicating that the integrated projections were constructed correctly.

To verify the accuracy of the Tensor Tomography (TT) reconstruction, we identified a rotation for the PPC-CT reconstructed volume that approximately aligns it with the XRD-TT reconstructed volume. In Fig. 3.9, two slices of the XRD-TT scalar volume (binary mask) and the PPC-CT rotated reconstruction in similar regions are shown, preliminary confirming that both techniques have reconstructed the same volume.

We can compare the PPC-CT reconstruction not only with the scalar volume but also with the orientation of the voxels. Fig. 3.10 plots similar regions for the XRD-TT reconstruction and PPC-CT reconstruction. The ordered orientation regions close to the edge seen on the XRD-TT slices match with the layered-like structures close to the edge of the PPC-CT reconstructed volume.

Based on the findings presented in this section, we can infer that the gallbladder stone sample used in the experiment is composed of cholesterol monohydrate crystallites. These crystallites have a tendency to align themselves with their long axis perpendicular to the

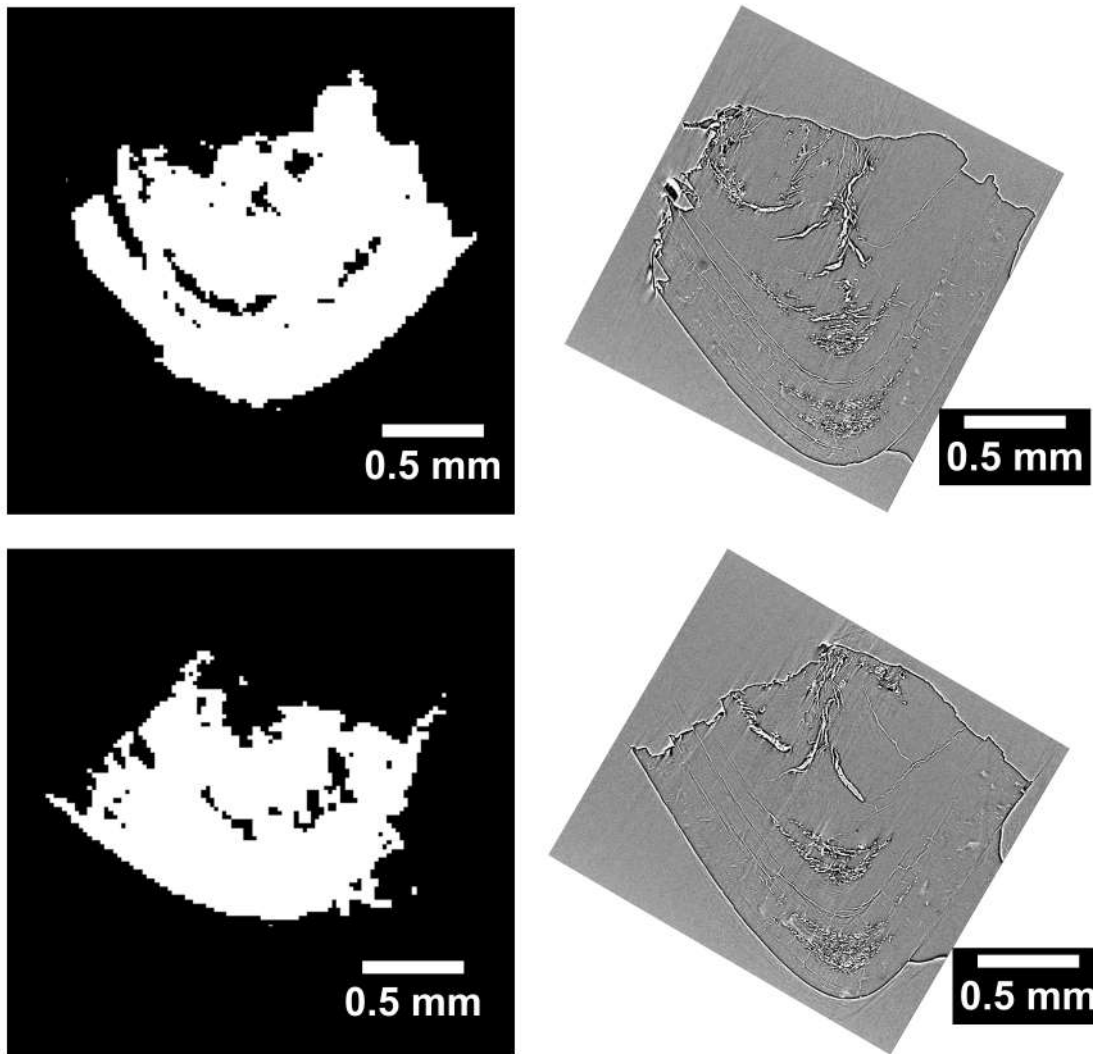


Figure 3.9: On the left side, two slices of the binary reconstructed volume with the Tensor Tomography technique. On the right side, two slices of the Computed Tomography reconstruction, rotated to approximately match the alignment of the Tensor Tomography reconstructed volume.



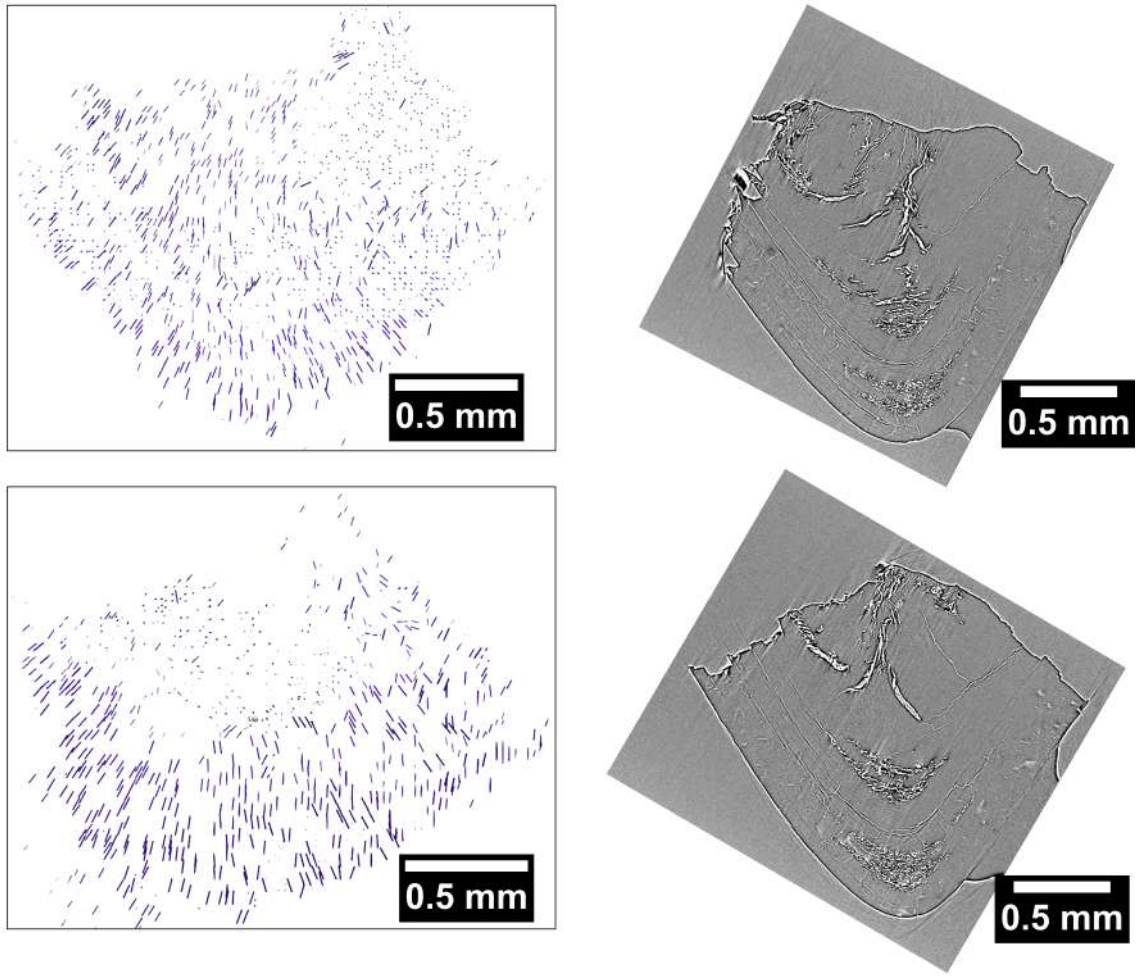


Figure 3.10: On the left side, two slices of the 3D visualization of the Tensor Tomography reconstruction. On the right side, two slices of the Computed Tomography reconstruction, rotated to approximately match the alignment of the Tensor Tomography reconstructed volume. The slices shown are the same as those in Fig. 3.9

edge of the volume, and exhibit a more flexible orientation towards the center of the stone.

## Chapter 4

# Conclusion

The research in this thesis focuses on using an X-ray Diffraction Tensor Tomography reconstruction technique to create a 3D image of a gallstone sample. This image provides information about the orientation of the cholesterol monohydrate crystals that form the gallstone. To validate the reconstruction and gain a better understanding of the sample's microstructure, we compared it with a Propagation-based Phase-Contrast Computed Tomography reconstruction.

As a result, we found that the cholesterol monohydrate crystals of the sample orient themselves with their long axis perpendicular to the edges of the sample. However, further analysis of the reconstructions could provide more information. For example, aligning both reconstructed volumes better and superimposing slices of one on top of slices of the other could help study if there is any special relation between the orientation of the crystals and their closeness to the cavities in the interior.

While there is no previous work applying XRD-TT reconstruction technique to gallbladder stone samples, its composition and morphology have been studied. The results of this thesis coincide with previous works when it comes to determining the composition of the gallstone by analyzing the diffraction patterns and resolving the internal structure of it with cavities and holes.

The detailed understanding of crystallographic orientation and internal morphology provided by XRD-TT and PPC-CT have provided us with the identification of preferred orientations and compositions. This information could be used to develop targeted therapies to disrupt these structures.

# Bibliography

- [1] Avinash C. Kak and Malcolm Slaney. *Principles of Computerized Tomographic Imaging*. IEEE PRESS, 1999.
- [2] Naomi E. Omori, Antonia D. Bobitan, Antonis Vamvakeros, Andrew M. Beale, and Simon D. M. Jacques. Recent developments in x-ray diffraction/scattering computed tomography for materials science. *Philosophical Transactions of the Royal Society A*, 381(20220350), 2023. URL: <http://doi.org/10.1098/rsta.2022.0350>, doi: [10.1098/rsta.2022.0350](https://doi.org/10.1098/rsta.2022.0350).
- [3] Philip J Withers, Charles Bouman, Simone Carmignato, Veerle Cnudde, David Grimaldi, Charlotte K Hagen, Éric Maire, Marena Manley, Anton Du Plessis, and Stuart R Stock. X-ray computed tomography. *Nature Reviews Methods Primers*, 1, February 2021. URL: <https://hal.science/hal-03544130>, doi: [10.1038/s43586-021-00015-4](https://doi.org/10.1038/s43586-021-00015-4).
- [4] Ilian Häggmark, William Vågberg, Hans M. Hertz, and Anna Burvall. Comparison of quantitative multi-material phase-retrieval algorithms in propagation-based phase-contrast x-ray tomography. *Opt. Express*, 25(26):33543–33558, Dec 2017. URL: <https://opg.optica.org/oe/abstract.cfm?URI=oe-25-26-33543>, doi: [10.1364/OE.25.033543](https://doi.org/10.1364/OE.25.033543).
- [5] Siwei Tao, Congxiao He, Xiang Hao, Cuifang Kuang, and Xu Liu. Principles of different x-ray phase-contrast imaging: A review. *Applied Sciences*, 11(7), 2021. URL: <https://www.mdpi.com/2076-3417/11/7/2971>, doi: [10.3390/app11072971](https://doi.org/10.3390/app11072971).
- [6] Fredrik Kristoffer Mürer. *Diffraction X-ray Tomography of Oriented Mineralized Structures in Hierarchical Materials*. PhD thesis, Norwegian University of Science and Technology, Department of Physics, 2021.
- [7] F.K. Mürer, S. Sanchez, M. Álvarez Murga, A. Rack, K.D. Knudsen, and A. Gourrier. 3d maps of mineral composition and hydroxyapatite orientation in fossil bone samples obtained by x-ray diffraction computed tomography. *Scientific Reports*, 8:10052, 2018. doi: [10.1038/s41598-018-28269-1](https://doi.org/10.1038/s41598-018-28269-1).
- [8] B. Chattopadhyay, A. S. Madathiparambil, F. K. Mürer, P. Cerasi, Y. Chushkin, F. Zontone, A. Gibaud, and D. W. Breiby. Nanoscale imaging of shale fragments with coherent x-ray diffraction. *Journal of Applied Crystallography*, 53(Pt 6):1562–1569, 2020. doi: [10.1107/S1600576720013850](https://doi.org/10.1107/S1600576720013850).
- [9] A. Gibaud, D. Younas, L. Matthews, T. Narayanan, K. Longkaew, I. U. Hageberg, Y. Chushkin, D. W. Breiby, and B. Chattopadhyay. Insights into the precipitation kinetics of  $\text{CaCO}_3$  particles in the presence of polystyrene sulfonate using *in situ*



- small-angle X-ray scattering. *Journal of Applied Crystallography*, 56(4):1114–1124, Aug 2023. doi:10.1107/S1600576723005356.
- [10] Marianne Liebi, Marios Georgiadis, Joachim Kohlbrecher, Mirko Holler, Jörg Raabe, Ivan Usov, Andreas M. Menzel, Philipp Schneider, Oliver Bunk, and Manuel Guizar-Sicairos. Small-angle x-ray scattering tensor tomography: model of the three-dimensional reciprocal-space map, reconstruction algorithm and angular sampling requirements. *Acta Crystallographica. Section A, Foundations and Advances*, 74:12 – 24, 2018. URL: <https://api.semanticscholar.org/CorpusID:28535213>.
  - [11] Dag W. Breiby and Emil J. Samuelsen. Quantification of preferential orientation in conjugated polymers using x-ray diffraction. *Journal of Polymer Science Part B: Polymer Physics*, 41(20):2375–2393, 2003. URL: <https://onlinelibrary.wiley.com/doi/abs/10.1002/polb.10624>, arXiv:<https://onlinelibrary.wiley.com/doi/pdf/10.1002/polb.10624>, doi:10.1002/polb.10624.
  - [12] Israel Hanukoglu. Steroidogenic enzymes: Structure, function, and role in regulation of steroid hormone biosynthesis. *The Journal of Steroid Biochemistry and Molecular Biology*, 43(8):779–804, 1992. URL: <https://www.sciencedirect.com/science/article/pii/S0960076092903075>, doi:10.1016/0960-0760(92)90307-5.
  - [13] Online etymology dictionary. <https://www.etymonline.com/word/cholesterol>. Accessed: 01-05-2024.
  - [14] National center for biotechnology information (2024). <https://pubchem.ncbi.nlm.nih.gov/compound/Cholesterol>. Accessed: 01-05-2024.
  - [15] Samiran Pramanik, Soumen Ghosh, Arkaprovo Roy, Ramanuj Mukherjee, and Alok Kumar Mukherjee. Phase composition and morphological analysis of human gallstones using ir spectroscopy, scanning electron microscopy and x-ray rietveld analysis. *Zeitschrift für Kristallographie - Crystalline Materials*, 231(2):97–105, 2016. URL: <https://doi.org/10.1515/zkri-2015-1881> [cited 2024-05-30], doi:doi:10.1515/zkri-2015-1881.
  - [16] Carlos Martínez Mingo. *Ultrastructure analysis of gallbladder stones using Computed Tomography*. PhD thesis, Norwegian University of Science and Technology, Department of Physics, 2020.
  - [17] Ingvild Uri Hageberg, Daniyal Younas, Fredrik K. Mürer, Katharina Scheidl, Kim Robert Bjørk Tekseth, Marco Di Michiel, Yuriy Chushkin, Dag W. Breiby, and Basab Chattopadhyay. Cholesterol gallstone ultrastructure revealed using x-ray phase contrast and diffraction tensor tomography.
  - [18] Dectris. Brochure - pilatus3 s and x. 2003.
  - [19] Doğa Gürsoy, Francesco De Carlo, Xianghui Xiao, and Chris Jacobsen. Tomopy: a framework for the analysis of synchrotron tomographic data. *Journal of Synchrotron Radiation*, 21:1188 – 1193, 2014. URL: <https://api.semanticscholar.org/CorpusID:17267081>.
  - [20] Daniël M. Pelt, Doğa Gürsoy, Willem Jan Palenstijn, Jan Sijbers, Francesco De Carlo, and Kees Joost Batenburg. Integration of TomoPy and the ASTRA toolbox for advanced processing and reconstruction of tomographic synchrotron data. *Journal of Synchrotron Radiation*, 23(3):842–849, May 2016. doi:10.1107/S1600577516005658.

- [21] F Edward Boas and Dominik Fleischmann. Ct artifacts: Causes and reduction techniques. *Imaging Med.* 4(2), 229-240, 2012.
- [22] M. Liebi, M. Georgiadis, A. Menzel, P. Schneider, J. Kohlbrecher, O. Bunk, M. Guizar-Sicairos, and P. Rüegsegger. Nanostructure surveys of macroscopic specimens by small-angle scattering tensor tomography. *Nature*, 527:349–352, 2015. [doi:10.1038/nature16056](https://doi.org/10.1038/nature16056).

